A Quality-Control Procedure for Bio-Optical Applications of Hyperspectral Radiometric Upwelling Radiance and Downwelling Irradiance Profiles Measured by BioGeoChemical-Argo Floats.

[a,b] Lou Andrès & [c] Charlotte Begouen Demeaux, [d] Emanuele Organelli, [d] Giovanni La Forgia, [c] Nils Haëntjens, [e,f] Vincenzo Vellucci, [a] Edouard Leymarie, [g] Catherine Schmechtig, [a] Antoine Poteau, [b] Antoine Mangin, [c] Emmanuel Boss, [a] Hervé Claustre

[a] *Sorbonne Université, CNRS, Laboratoire d'Océanographie de Villefranche, LOV, F-06230 Villefranche-sur-Mer, France*

[b] *ACRI-ST, Sophia-Antipolis, France*

[c] *University of Maine, School of Marine Sciences, Aubert Hall, Orono, Maine*

[d] *National Research Council of Italy (CNR), Institute of Marine Science (ISMAR), Rome, Italy*

[e] *Sorbonne Université, CNRS, Institut de la Mer de Villefranche, IMEV, Villefranche-sur-Mer, F-06230, France*

[f] *Sorbonne Université, CNRS, OSU Station Marines, STAMAR, Paris, F-75006, France*

[g] *OSU Ecce Terra, UMS 3455, CNRS and Université Pierre et Marie Curie, Paris, France*

Corresponding authors: Lou Andrès, lou.andres@imev-mer.fr

& Charlotte Begouen Demeaux, charlotte.begouen@maine.edu

A Quality-Control Procedure for Bio-Optical Applications of Hyperspectral Radiometric Upwelling Radiance and Downwelling Irradiance Profiles Measured by BioGeoChemical-Argo Floats.

[a,b] Lou Andrès & [c] Charlotte Begouen Demeaux, [d] Emanuele Organelli, [d] Giovanni La Forgia, [c] Nils Haëntjens, [e,f] Vincenzo Vellucci, [a] Edouard Leymarie, [g] Catherine Schmechtig, [a] Antoine Poteau, [b] Antoine Mangin, [c] Emmanuel Boss, [a] Hervé Claustre

[a] *Sorbonne Université, CNRS, Laboratoire d'Océanographie de Villefranche, LOV, F-06230 Villefranche-sur-Mer, France*

[b] *ACRI-ST, Sophia-Antipolis, France*

[c] *University of Maine, School of Marine Sciences, Aubert Hall, Orono, Maine*

[d] *National Research Council of Italy (CNR), Institute of Marine Science (ISMAR), Rome, Italy*

[e] *Sorbonne Université, CNRS, Institut de la Mer de Villefranche, IMEV, Villefranche-sur-Mer, F-06230, France*

[f] *Sorbonne Université, CNRS, OSU Station Marines, STAMAR, Paris, F-75006, France*

[g] *OSU Ecce Terra, UMS 3455, CNRS and Université Pierre et Marie Curie, Paris, France*

Corresponding authors: Lou Andrès, lou.andres@imev-mer.fr

& Charlotte Begouen Demeaux, charlotte.begouen@maine.edu

ABSTRACT

Autonomous in-situ radiometric observations are increasingly used to constrain bio-optical processes and validate satellite ocean-color products, such as remote sensing reflectance and diffuse attenuation coefficients. Because these observations are collected independently of weather and sea-state conditions, their application critically depends on robust quality control.

Starting in 2012, the BioGeoChemical-Argo (BGC-Argo) program has measured downwelling irradiance (E_d) at three wavelengths on autonomous floats. Since 2022, a pilot array of 12 BGC-Argo floats equipped with TriOS-RAMSES hyperspectral radiometers measuring E_d and upwelling radiance (L_u) has been deployed across open-ocean regions with diverse bio-optical properties. To date, these floats have acquired hundreds of hyperspectral profiles from 0–300 m at ~10-day intervals near local noon.

This study presents an automated Quality Control (QC) method for hyperspectral E_d and L_u profiles measured by BGC-Argo floats, building upon previous QC procedures designed for multispectral radiometry. The method flags perturbations in the light field caused by self-shading, large tilt angles, passing clouds, wave focusing, spikes, and corrects for dark current signals. The QC is first applied at five key wavelengths (380, 443, 490, 555, and 620 nm) to generate wavelength-specific flags along each vertical profile, which are then combined into a final global classification for each spectral profile as *Good*, *Questionable*, or *Bad*.

This paper, along with its Python code and data files, provides the community with a robust and computationally efficient approach for assessing hyperspectral BGC-Argo data quality, preparing it for further bio-optical applications.

1. Introduction

Since its inception in the early 2000s, the Argo program has maintained approximately 4,000 autonomous floats across the world's oceans. These floats measure pressure, temperature, and salinity, profiling from a depth of 2,000 meters to the surface every 10 days. After each cycle, the collected data are transmitted by satellite to land before the float begins a new sampling cycle. This unprecedented collaboration among 30 countries resulted in the collection of over 2 million profiles of ocean parameters, revolutionizing the scientific community's understanding of climate systems, weather forecasting, circulation, and more (Roemmich et al., 2019; Wong et al., 2020).

In 2016, the Argo program was expanded to include measurements of biogeochemical variables (Bittig et al., 2019; Johnson & Claustre, 2016). The BioGeoChemical-Argo (BGC-Argo) initiative aims to maintain a network of ~1,000 floats that, in addition to the core Argo parameters, measure dissolved oxygen, nitrate, pH, phytoplankton chlorophyll-a, optical backscattering coefficient, photosynthetically available radiation (PAR), and downwelling irradiance (E_d), providing critical insights into the ocean's biological and chemical processes (Claustre et al., 2020). These BGC-Argo floats follow the same sampling cycle as Argo floats, sampling every 10 days from 2,000 meters up to the surface, except the radiometric parameters (E_d and PAR) that are collected in the upper 300 meters.

Starting in 2022, as part of the ERC-funded REFINE (Robots Explore plankton-driven Fluxes in the marine twIlight zoNE) project, a subset of these floats has been equipped with ruggedized hyperspectral TriOS-RAMSES G2 radiometers to measure profiles of both E_d and upwelling radiance (L_u) at at least 70 wavelengths. These hyperspectral BGC-Argo floats will hereafter be referred to as *hyperspectral floats*. Twelve of these floats are operational and acquire data in near real time across open-ocean regions representative of the ocean's diverse bio-optical conditions. This hyperspectral fleet, programmed to reach the surface at local noon, provides a new in situ data source for bio-optical applications and validation of hyperspectral satellite ocean color missions such as NASA's newly launched Plankton, Aerosol, Cloud, Ocean Ecosystem (PACE) satellite (Werdell et al., 2019).

Raw radiometric data need to be processed to identify perturbations in the light field (e.g., self-shading, float tilt, wave focusing, passing clouds, etc.) that limit their utility for bio-optical applications. Quality control (QC) procedure for radiometric quantities measured by autonomous floats has already been designed for E_d acquired by SeaBird-OCR radiometers mounted on floats (Organelli et al., 2016; Wojtasiewicz et al., 2018). Earlier QC procedures were developed for multispectral radiometers measuring only three discrete bands, typically selected from 380, 412, 443, 490, and 555 nm. Because these instruments did not sample wavelengths longer than 555 nm, the original QC framework was neither designed nor evaluated for the yellow–red region of the spectrum. In contrast, hyperspectral radiometers cover a much broader spectral range, extending approximately from 320 to 780 nm. This spectral region includes key optical features such as chlorophyll fluorescence and Raman scattering (Bartlett et al., 1998; Bricaud et al., 2004; Desiderio, 2000), as well as strong absorption by water, complicating quality assessment. Consequently, an updated QC procedure is required to reliably detect artifacts—such as wave-focusing effects—at these longer wavelengths. This updated method needs to be computationally efficient, applicable to both E_d and L_u, and relies solely on these 2 variables to be effective across the entire visible spectrum and the entire hyperspectral fleet.

This study, therefore, aims to build upon the previous QC procedures developed for BGC-Argo multispectral radiometry and adapt them to hyperspectral TriOS-RAMSES G2 measurements.

It functions by first assessing individual data points along depth within a profile at five key wavelengths (380, 443, 490, 555, and 620 nm). For the rationale of the key wavelength selection, please see Section 3.a. Based on these QC by wavelengths, the whole spectrum is then characterized and given one overall flag, but there is no data correction or removal.

This QC procedure has been developed and tested on 899 profiles available from 12 BGC-Argo floats, profiling in various open ocean regions in the period since June 2022. It is important to note that this procedure is not designed to be implemented in the BGC-Argo Global Data Assembly Center (GDAC). Indeed, data distributed from the GDAC (both in digital counts and in scientific units) only aim to be free of sensor issues. In contrast, the QC presented here is an additional procedure that relies on data delivered by GDAC in order to detect light field disturbances in the signal (e.g., passing clouds). This enables users to efficiently quality control spectra that can be used for bio-optical applications such as ocean color radiometry validation or diffuse light attenuation coefficient (K_d/K_L) computation. Therefore, there is a fundamental difference between data post-GDAC quality control (free of sensor issues but not necessarily usable for bio-optical applications) and the output from the quality control presented in this paper (free of sensor issues *and* usable for bio-optical applications).

2. Instruments and data

a. Hyperspectral data

A new generation of BGC-Argo floats has been designed in the context of the ERC-REFINE project. The platform (NKE Provor CTS5 Jumbo, Fig. 1) enables the integration of two hyperspectral radiometers (TriOS RAMSES G2), one measuring E_d and the other L_u, along with various optical sensors such as a fluorometer, a backscattering sensor, a transmissometer, and an Underwater-Vision-Profiler (UVP6). To reduce shading effects, the E_d and L_u sensors are mounted respectively at the top of the float and at the very bottom (each sensor collector is respectively 0.50 m above the waterline and 1.76 m under the waterline when the float is at the surface). However, at specific sun azimuth angles (saa), L_u measurements can still be shaded by the float body and thus require a specific processing (see details in Section 3.c).

This study uses 899 profiles collected by 12 floats between June 2022 and June 2025 in various oceanic areas (Fig. 1). Raw data are publicly available online at ftp://ftp.ifremer.fr/ifremer/argo/aux/coriolis/.

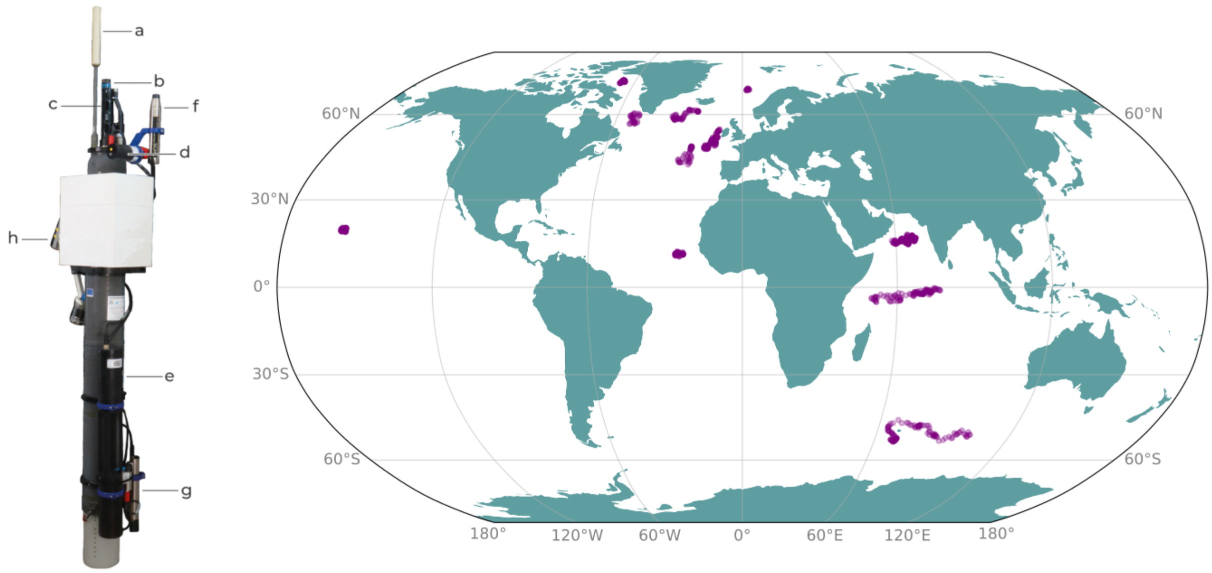

Fig. 1. On the left panel: the PROVOR CTS-5 profiling float equipped with (a) Iridium antenna; (b) oxygen sensor; (c) conductivity–temperature–pressure sensor; (d) sensor measuring chlorophyll-a fluorescence, dissolved organic matter fluorescence, and light backscattering; (e) transmissometer; (f) hyperspectral downwelling irradiance radiometer (E_d); (g) hyperspectral upwelling radiance radiometer (L_u); (h) Underwater Vision Profiler (UVP). Photo by Thomas Jessin and Thomas Boniface. On the right panel: map of the profiles used in this study. Each circle corresponds to a location where hyperspectral radiometric profiles of E_d and L_u were measured, for a total of 899 float profiles.

b. Technical specs: TriOS hyperspectral radiometers

The E_d radiometers (RAMSES G2-**ACC**-VIS-Ti-2000m) have a cosine collector of 3.5 mm in radius. L_u radiometers (RAMSES-G2-**ARC**-VIS-Ti-2000m) have a 7° full-angle Field Of View (FOV) in air. Both have a 256-channel (or -pixel) detector with a Full Width Half-Max of 9.5 nm, including ~17 darkened pixels, and spectral sensitivity coefficients were determined by the manufacturer on individual sensors pre-deployment (TriOS, 2024). Immersion coefficients were laboratory-determined by the manufacturer for each **ACC**-type sensor and theoretically for **ARC**-type sensors (Ohde & Siegel, 2003). Following the TriOS user manual, the integration time is automatically set between 4 ms and 4096 ms: a first scan is performed at 4096 ms; if any of the pixels is saturated, a second scan is performed with a new integration time equal to half of the previous one (here: 4096/2 = 2048 ms), and so on until one of the pixels is saturated. Detailed sensor specifications can be found in Vabson et al. (2024). TriOS sensors are equipped with an internal tilt sensor that takes a measurement before and after each spectrum. In this study, the post-tilt measurement is used as the tilt value because it is the closest in time to the spectral acquisition.

Measurements are collected during the upward casts, programmed every 10 days, with the first spectrum taken at the parking depth (1,000 m). During the 4 months of the initial acquisition phase of the PACE satellite, the measurements were acquired every 5 days. Radiometric data are recorded by the float from ~300 m depth to the surface with a vertical resolution rising from 10 to 0.3 m as the float ascends: 4 points per meter between the surface and 20 m, 1 point per meter between 20 to 100 m, 1 point every 2 meters from 100 to 200 m and 1 point every 5 meters from 200 to 300 m. The floats therefore have a relatively low vertical resolution - less than 4 points per meter compared to ~15 points per meter for other known systems (HyperPro, C-OPS, HyperNav, Zibordi et al., 2019). Combined with the fact that there is only a single upward profile per cycle, mitigation strategies such as multicasting cannot be used to reduce wave perturbations (Zibordi et al., 2004). Thus, BGC-Argo data requires a specific QC capable of detecting data affected by wave focusing. Concurrent dark measurements are collected on ~17 “black” detector channels consisting of purposely masked detector pixels.

All hyperspectral BGC-Argo floats are programmed to reach the surface at local noon. For the PROVOR floats, the hyperspectral measurements are transmitted from 320 to 780 nm at the original 3.3 nm spectral sampling or binned at 6.6 nm (a two-by-two channels average), depending on the float’s configuration (TriOS, 2025). The central wavelength associated with each pixel slightly varies (<4 nm) between sensors, meaning that all hyperspectral radiometers from the fleet do not have the same distribution of spectral bands.

c. Processing of raw data.

Electronic raw counts are transmitted to land through a two-way Iridium satellite communication, which also enables the remote adjustment of mission and sensor parameters (sampling frequency, pixel binning, drift duration, drift depth, detector channel start, detector channel stop). Radiometric quantities are then retrieved following the TriOS recommendations (TriOS, 2025), detailed in Appendix A.

E_d and L_u data in physical units (respectively W m^{-2} nm^{-1} and W m^{-2} nm^{-1} sr^{-1}) are available at ftp://ftp.ifremer.fr/ifremer/argo/.

3. Quality control protocol

The following section details the different steps of the QC protocol specifically adapted for hyperspectral floats. It should be noted that this QC procedure and flags are not equivalent to those applied as part of the standard Argo data quality framework. Argo real-time QC applies a suite of automatic tests to core physical and biogeochemical variables (e.g., global range check, pressure gradient, spikes), aiming at identifying only if the instrument performance is satisfactory (Poteau et al., 2019). Thus, multispectral E_d data are not subject to screening for light perturbations such as wave focusing. Instead, this present QC evaluates the light environment at the time of the measurements, which can affect the subsequent derivation of optical quantities (e.g., remote sensing reflectances and diffuse attenuation coefficients), a need previously identified (Claustre et al., 2020). Building on previously published QC approaches for multispectral radiometry (Organelli et al., 2016; Wojtasiewicz et al., 2018), this method is designed for hyperspectral radiometers to detect the occurrence of passing clouds, self-shading, large tilt angles, wave-focusing effects, and spike events along a profile, without attempting to attribute these perturbations to their physical causes.

The first QC step is to determine whether the profile is acquired at daylight and flag data points where the tilt angle of the float remains below 5° (Zibordi et al., 2019). Then, the method distinguishes the section of the profile containing a radiometric signal from the section dominated by instrument noise (i.e., dark current). Quality control will only be applied on the “signal layer” (i.e., the layer where the signal is significantly greater than zero), which varies over wavelengths, time of day, and water composition. As a result, the depth at which the QC is performed will differ across profiles and wavelengths. The QC protocol begins with a check of individual data points, followed by verification of the vertical profile shape at five “reference” wavelengths—380, 443, 490, 555, and 620 nm (see Section 3.b for justification), and each obtains a wavelength-specific quality flag after two successive 4th degree polynomial fits and an optional shaded data filter on L_u measurements only. The first polynomial fit detects passing clouds and large spikes, whereas the second one, applied on data points without residuals from the fit, flags weaker perturbations such as wave focusing (Organelli et al., 2016). The last step is to assign a final flag to the full hyperspectral profile.

The overall procedure is summarized in Fig. 2. Following the convention defined in Organelli et al. 2016, for each wavelength, three profile types are introduced. “type 1” qualifies good profiles, that can readily be used for bio-optical applications, “type 3” qualifies bad profiles, affected by environmental disturbances, while “type 2” corresponds to “questionable” profiles, with potentially usable measurements for bio-optical application but who could require some case-by-case additional processing/data manipulation (see examples in Fig. 3).

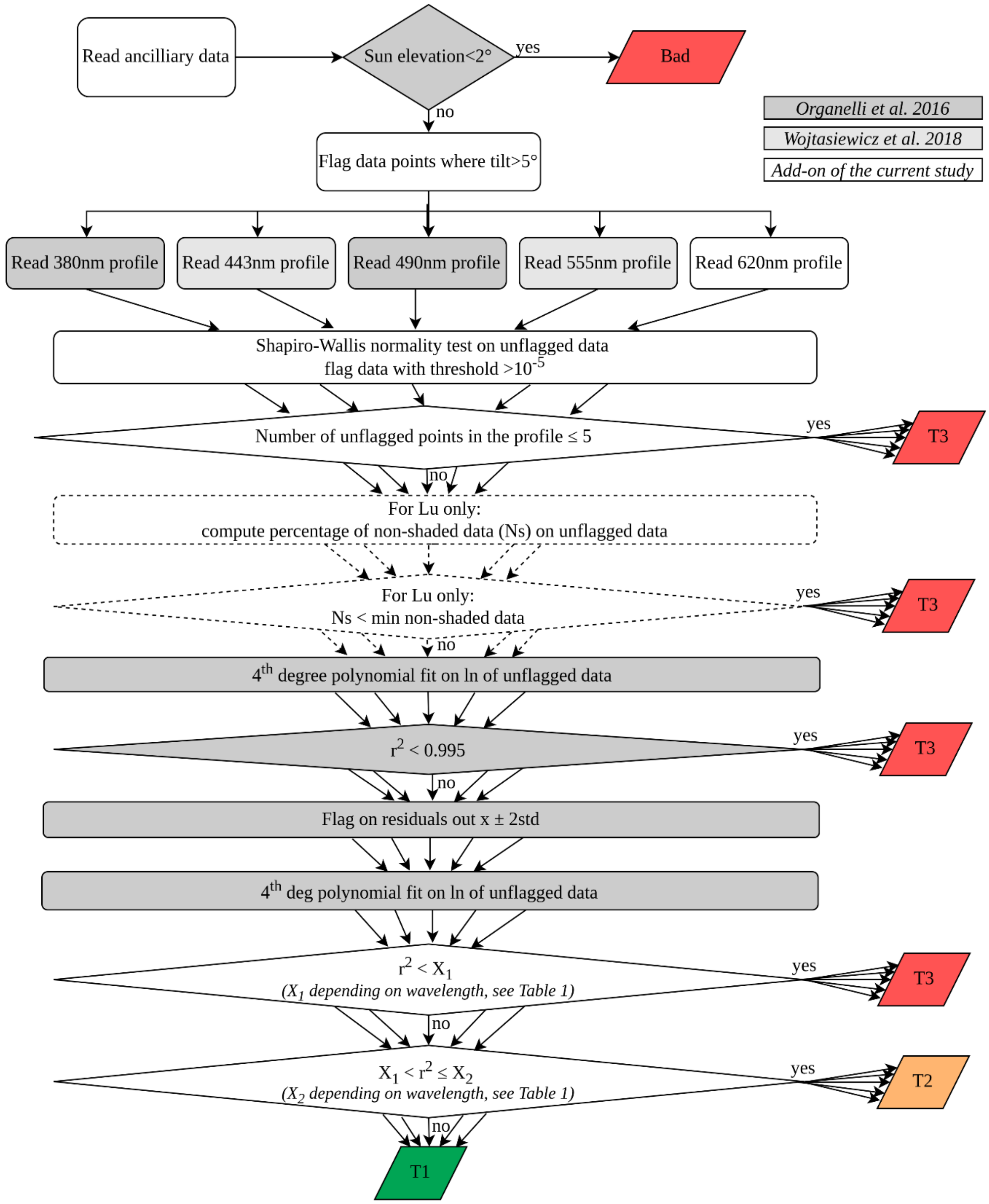

Overall quality of the spectrum

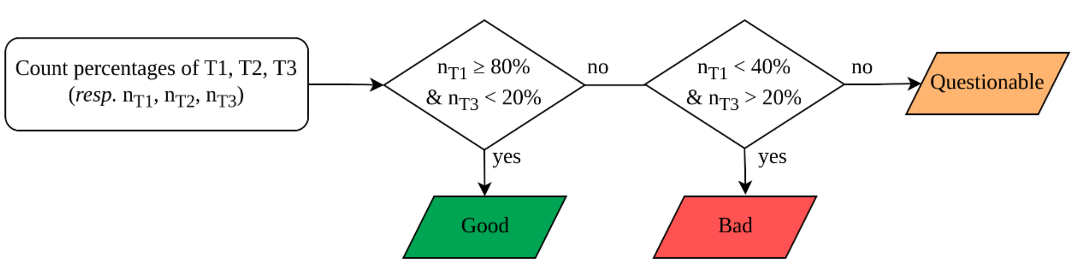

Fig 2: Flowchart of the QC procedure for hyperspectral data with the same conventions as in (Organelli et al., 2016): ‘‘x’’ is the mean of residuals, and T1, T2, T3 refer to the profile “type”. For the last step, “n_{Ti}” refers to the number of wavelengths with a given type. The colors of the boxes refer to the method from which the step is taken: Organelli et al., 2016 (dark gray), Wojtasiewicz et al., 2018 (light gray), and the QC procedure described in this paper (white).

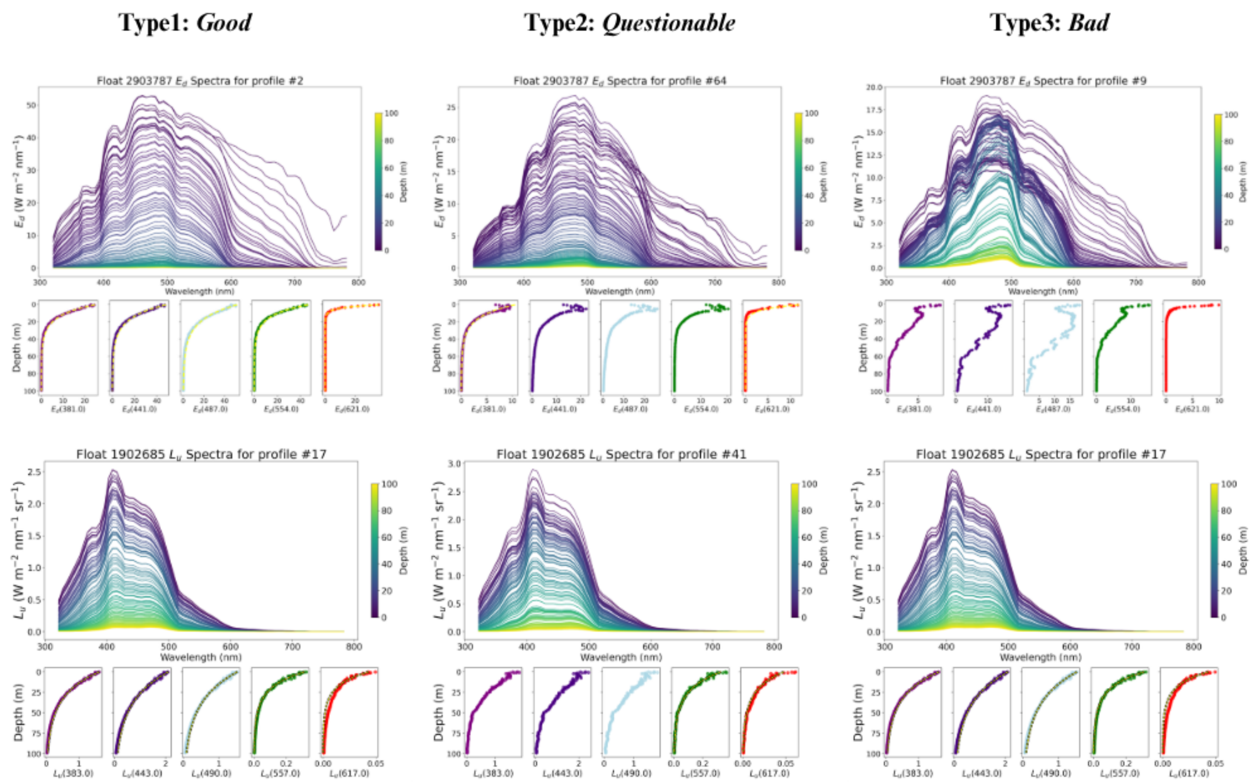

Fig 3: Top row: Example of the three different E_d profile types acquired by float WMO 2903787. On the left-hand side at the top, a type 1 “Good” profile. Type 2 profile is in the middle, with some wave-focusing at the intermediate wavelengths. On the right side, a type 3 “Bad” profile, likely affected by passing clouds. In dashed yellow, the 4th degree polynomial fit to each wavelength’s E_d profile, on a linear scale, from the computed K_d (only computed when the wavelength is classified as type 1 or type 2). On the bottom row: three different L_u profile types acquired by float WMO 1902685. Same order as for the E_d profiles, with, from left to right, type 1 to type 3 classification.

a. Selection of the different wavelengths

Although the present QC procedure is designed for hyperspectral data, it is performed on a subset of wavelengths, ensuring robust quality control while achieving computational efficiency. The comparison with a full hyperspectral QC approach is discussed in Section 4.e. The reference wavelengths were selected based on those adopted by the BGC-Argo community for multispectral float measurements and those typically used by satellite ocean-color missions (e.g., Sentinel-3 OLCI, MODIS-Aqua, VIIRS). The 380 nm and 490 nm wavelengths are used for the QC in Organelli et al. (2016) and correspond to two of the channels on the multispectral E_d sensor from the BGC-Argo program (OCR-504, Sea-Bird Scientific). 443 nm and 555 nm are used in the QC of Wojtasiewicz et al. (2018) for both L_u and E_d and will be on the new version of multispectral E_d sensors adopted by the BGC-Argo community. The last wavelength (620 nm) is used to evaluate the red part of the visible spectrum. The specific 620 nm value matches the Sentinel-3 OLCI red band (Oa7, Donlon et al., 2012). In practice, since the wavelengths can differ by about 4 nm between radiometers, the sensor's wavelength closest to each reference wavelength is selected.

b. Wavelength-specific signal layer detection

The depth range over which QC is applied varies by wavelength, as light attenuates differently at different wavelengths. To ensure consistency, QC is performed over the full depth range over which a light signal is detected for each wavelength. To differentiate the environmental dark signal from the light signal, a normality test was performed on the data, as dark values are normally distributed as a function of depth, whereas light measurements are not (Organelli et al., 2016). We define z_{dark} as the threshold depth, corresponding to the level below which light is effectively negligible. During the gradual shift from very low light levels to darkness, the light is not necessarily completely null around $z_{dark.}$ Assuming z_{dark} as the dark threshold potentially leads to the exclusion of a small portion of the profile, although this portion has a negligible amount of light. Following La Forgia & Organelli (2025), the Shapiro-Wilk test (Shapiro & Wilk, 1965) of normality was applied to all the selected bands with a p-value threshold of 10^{-5}, as the Lilliefors test (Thode, 2002) adopted by Organelli et al. (2016) was not sensitive enough for the 620 nm band, resulting in lower sections of the profile flagged as light when they corresponded to a dark signal (Fig. 4). The Shapiro–Wilk test evaluates whether a set of values is drawn from a normally distributed population. It is based on comparing the ordered sample values to the expected values of a normal distribution using a correlation-type statistic (the p-value). A high p-value, therefore, indicates that the distribution of values is statistically indistinguishable from Gaussian noise, i.e., the depth range where the signal becomes dominated by instrumental dark current. In practice, the Shapiro-Wilk test was processed iteratively: for each pressure level P* associated with a spectrum, the p-value was derived from all the data points associated with a pressure higher than P* (data from greater depth where less light is expected). This profile-by-profile approach has the advantage of being dependent on data distribution only, avoiding noise equivalent irradiance (NEI) estimation or sensor sensitivity drift issues.

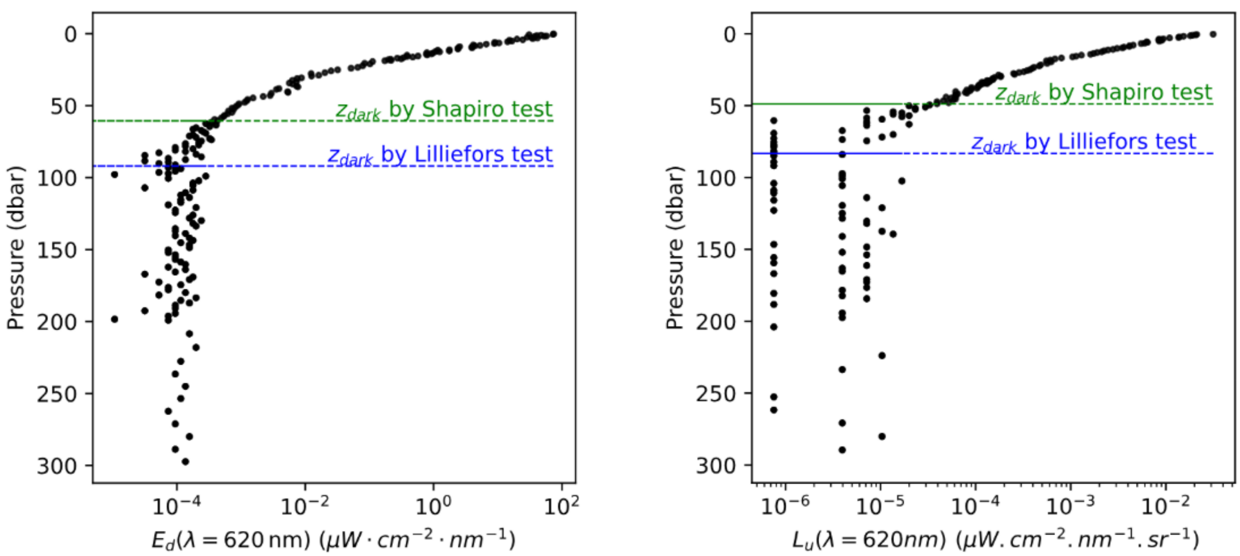

Fig. 4. Comparison of the two dark detection methods on the E_d profile N° 58 at 620 nm of the float WMO 1902637 (black dots) (left panel) and on the L_u profile N°10 at 620 nm of the float WMO 1902637 (right panel). The dashed lines indicate the limit depth (z_{dark}) between the "signal" layer and the dark layer. Both z_{darks} are derived from statistical tests for normality of data: Lilliefors test (Thode, 2002) in blue and Shapiro-Wilk (Shapiro & Wilk, 1965) in green.

c. Detection of shaded points (L_u specific steps)

Due to the float geometry, L_u measurements are strongly dependent on solar azimuth angle. Ensuring data quality therefore requires the ability to identify shaded measurements. For this reason, all hyperspectral floats are equipped with an inertial measurement unit (IMU) that includes a compass providing the heading, defined as the angle between float north and the magnetic north (resp. black and purple arrows, Fig. 5). Float north is defined by the manufacturer and aligned with the UVP sensor. Compass measurements are recorded as digital counts and stored alongside the radiometric data, along with the equations needed to convert them to physical units and correct for magnetic deviation (i.e. error of the compass caused by local magnetic field created by the float, see details in Appendix B). The Python scripts accompanying this paper compute the solar azimuth angle relative to geographic north. To align the reference frames, the magnetic declination—defined as the angle between geographic and magnetic north (resp. red and purple arrows, Fig. 5)—is derived using the World Magnetic Model 2020 (NOAA NCEI, 2024) and applied to convert the measured heading to a geographic north–referenced orientation. Finally, using the known angle between the radiance sensor and the float north provided by the manufacturer (135°, Fig. 5), data points for which the radiometer is on the sunny side of the float can be identified following the equation below:

$$\mathit{sun\ azimuth\ angle} - (\mathit{heading} + \mathit{magnetic\ declination})\ \epsilon\ [45°; 225°]$$

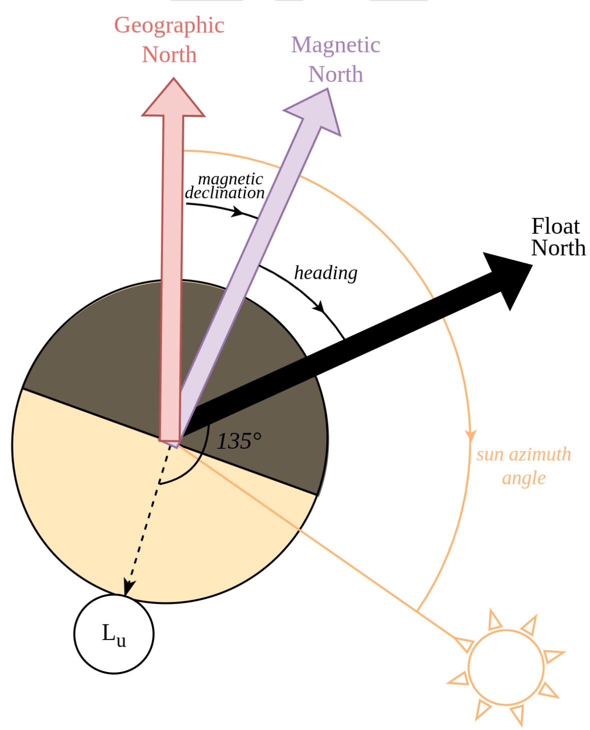

Fig. 5. View from above a hyperspectral float. When the Sun lies within the yellow sector of the circle (representing the float body), the measurements are considered non-shaded. When the relative orientation of the float and the Sun places the Sun within the dark sector, the corresponding L_u data are flagged as shaded by the float's body. The Sun's position relative to the float's North (black arrow) is calculated as the solar azimuth angle (saa) minus the sum of the

float heading (i.e. the angle between magnetic and float north, which relies on the compass measurement) and the magnetic declination (i.e. the angle between geographic and magnetic north).

Although the presented method flags shaded data points and allows users to specify a minimum acceptable number of non-shaded measurements throughout the profile (below which a profile is classified as Bad), the results presented hereafter in this paper follow the recommendations of Gerbi et al. (2016) by retaining all data points, both shaded and non-shaded, to preserve sufficient data density.

d. Revision of the coefficients for profile type assignment

Once z_{dark} has been estimated by the Shapiro-Wilk method, all data below this depth are flagged and will be ignored further in the QC processing. The same method developed by Organelli et al. (2016) is applied to identify moving clouds, wave focusing, and spikes: a 4th-degree polynomial fit on the Napierian logarithm (ln) of E_d and L_u, followed by the analysis of r^2 and the residuals of the difference between the polynomial fit and the data points (Fig. 2 and Fig. 3).

The threshold values for r^2 and residuals to determine the flag of each datapoint are wavelength-dependent, but apply to both E_d and L_u. The original QC threshold values for the 380, 443, 490, and 555 nm wavelengths are preserved (Organelli et al., 2016; Wojtasiewicz et al., 2018). At 620 nm, we slightly relaxed the criteria by choosing a threshold of 0.995 for the lower limit and 0.998 for the upper limit of type 2. This change accounts for a less robust polynomial fit in the red wavelengths because of the presence of inelastic scattering and the reduced light signal due to a stronger attenuation by water, which lowers the signal-to-noise ratio (see Section 4.c.). Thresholds are summarized in Table 1.

Band / Flag	X_1	X_2
380 nm	0.997	0.999

443 nm	0.996	0.998
490 nm	0.996	0.998
555 nm	0.996	0.998
620 nm	0.995	0.998

Table 1. Thresholds of r^2 used for the profile type identification for each wavelength. X1 and X2 denote the lower and upper limits of r^2, respectively (see Fig. 2).

e. Overall quality of the hyperspectral profile

Once each of the 5 wavelengths is assigned to a "type", the overall quality of the spectrum is determined based on the frequency of each of the three "types". Each criterion is detailed below and in the last step of the flowchart (Fig. 2), and an example of spectra corresponding to each type is available in Fig. 3. To summarize:

- If 80% or more of the reference wavelengths' profiles are categorized as "type 1" and less than 10% as "type 3", the radiometric profile (the hyperspectral E_d or L_u profile) is labeled as "Good".
- If more than 20% of the reference wavelengths' profiles are categorized as "type 3" and less than 40% as "type 3", the radiometric profile is flagged as "type 3" (Bad).
- For all other cases, type 2 is used by default, i.e. the data quality is considered "Questionable".

f. An extension to a hyperspectral method

To analyze whether this 5-wavelengths approach (called 5-QC hereon) is sufficient to spectrally qualify a given radiometric profile from 320 to 780 nm, we compared the results of the proposed

QC method with a hyperspectral version of it (called Hyper-QC hereon). The Hyper-QC characterizes profiles for every single wavelength available. The above-mentioned criteria were thus adapted to obtain the Hyper-QC approach. Correlation coefficient thresholds depend on whether wavelengths are shorter or longer than 600 nm. Details are presented in Table 2.

λ / Flag	X_1	X_2
$\lambda < 600$ nm	0.997	0.999
$\lambda \geq 600$ nm	0.995	0.998

Table 2. Thresholds of r^2 used in profile type identification for the Hyper-QC approach. X1 and X2 denote the lower and upper limits of r^2, respectively.

Once all wavelengths for a given radiometric profile are quality controlled, an overall quality flag is assigned to the whole profile, following the same criteria as the 5-QC described above, but only applied to wavelengths <650nm. Note that the number of wavelengths can vary between hyperspectral floats depending on the sampling channels' settings.

The overall Hyper-QC procedure follows the same steps as the 5-QC procedure, presented in Fig.2, with differences only in the threshold values.

4. Results and Discussion

The development of hyperspectral sensors will significantly enhance our ability to detect bio-optical features, such as chlorophyll absorption bands, fluorescence peaks, and Raman scattering, that multispectral instruments cannot resolve (Jemai et al., 2021; Organelli et al., 2021). Ensuring the quality of these full-spectrum measurements is critical for validating upcoming hyperspectral satellite missions (e.g., PACE) and for deriving spectral products such as hyperspectral Kd, spectral reflectance, and pigment-specific absorption metrics. Therefore, a QC procedure encompassing the full hyperspectral range enables robust identification of wavelength-dependent perturbations in the light field. This, in turn, increases confidence in applications that leverage the hyperspectral capability of the measurements.

We elected to use the same curve-fitting QC-based methodology for both E_d and L_u. Indeed, applying a QC originally designed for E_d to L_u is justified given that perturbations in the light field affect both E_d and L_u (albeit differently). Additionally, polynomial and regression-based screening of hyperspectral L_u profiles is already used in autonomous systems supporting satellite calibration (e.g., HyperNav, Barnard et al., 2024). A further discussion on the difference in QC result between the two variables can be found below in Section 4.c.

a. Quality of the profiles with the 5-QC

A total of 899 radiometric profiles from a large diversity of ocean regions and weather conditions (Fig.1) were QC-ed with the methods presented in section 3: for the E_d spectra, ~31% of the profiles were labeled as type 1 (ie: “Good”), 33% of the spectra are considered “Questionable” and ~37% are qualified as “Bad” (Fig. 6). For L_u, 33% of hyperspectral profiles were type 1, 31% type 2, and 35% were identified as type 3.

Fig. 6. Distribution of E_d profile (upper panel) and L_u profile (lower panel) types for each wavelength and for the overall hyperspectral profile.

There are two ways in which a profile can show variability in the 5-QC method: between the different wavelengths of the same radiometric profile (inter-wavelength variability, discussed in 4.b) or between E_d and L_u profiles that are measured simultaneously (discussed in 4.c).

b. Inter-wavelength variability

Significant variability in 5-QC classification exists across wavelengths of a given measurement (Fig. 6). Importantly, this variability does not indicate that certain spectral regions are unsuitable for the 4th-order polynomial test. Rather, it reflects wavelength-dependent differences in the physical and biological processes shaping the radiometric profiles, which motivates the use of wavelength-dependent r^2 thresholds when discriminating between quality levels. This can be explained by the predominantly oligotrophic nature of the waters sampled by the floats, with a strong signal in the blue-green region (443, 490, and 555 nm in this study), penetrating deep into the water column (Morel et al., 2007; Pope & Fry, 1997). Consequently, at those wavelengths, the QC is often performed over greater depths, increasing the number of available data points for the polynomial fitting and effectively reducing the impact of outliers near the surface on the fits performance. On the other hand, the float spends more time in the “signal” layer (as opposed to the dark layer where the QC is not performed), increasing the likelihood of weather perturbations (e.g., passing clouds).

Phytoplankton absorbs significantly more light at 490 nm than at longer wavelengths like 555 nm (Bricaud et al., 1995; Mobley, 2022). E_d profiles at 490 nm are therefore more susceptible to variations caused by the float crossing the Deep Chlorophyll Maximum (DCM), leading to changes in K_d. These changes can introduce an uneven decrease of E_d with depth as it moves across water masses with different phytoplankton concentrations, ultimately degrading the fit quality.

For L_u, the largest number of type 3 profiles is for the red wavelength. In the red wavelengths, absorption of light by pure water is strong, and most of the light disappears in the first few meters. The resulting shape of the L_u profile is therefore different than at other wavelengths, resulting in lower performance of the polynomial fit, regardless of biology and instrument performance. As phytoplankton naturally fluoresces with a relative maximum at ~685 nm (Gordon, 1979), the L_u profile shape can deviate from log-normal linearity for the wavelengths around, such as our reference wavelength at 620 nm, which contributes to explain why polynomial fit performances can be affected. Lastly, the red wavelengths are affected by Raman scattering, an inelastic scattering process where the incident blue light excites water molecules. As the water molecule decays post-excitation, it emits light at a longer wavelength (lower energy), i.e., in the visible spectrum's red wavelengths (Mobley, 2022). Therefore, the overall L_u/E_d profile is affected not only by constituents present in the water but also by a combination of pure water absorption, phytoplankton fluorescence, and Raman scattering. Those additional processes do not follow the same exponential decrease with depth, therefore the red wavelength can not be described by the polynomial fit as accurately as other wavelengths.

c. E_d versus L_u variability in QC type

Although E_d and L_u are measured almost simultaneously but with two different sensors, we recommend performing independent QC on each hyperspectral profile. As a result, the same float radiometric cast can be assigned two different types, depending on whether looking at the L_u or the E_d sensor data. The new QC analysis resulted in around 65% of profiles being assigned to the same type for the E_d and L_u (green boxes in Fig. 7) and 35% of differences, including 3.9% of these profiles exhibiting a type 3/type 1 discrepancy (red boxes in Fig. 7). These differences, depending on which sensor is QC-ed, are primarily due to two reasons. First, E_d corresponds to the light going downward, hence the sensor points upward, toward the sky. When the float is close to the surface, the E_d sensor is more sensitive to wave focusing (Gege & Pinnel, 2011) than the L_u sensor (which points downward). This can affect the r^2 coefficient of the polynomial fit, thus degrading the profile "type" of E_d as compared to L_u, especially in the blue (443 and 490 nm channels). As such, the percentages of type 1 profiles for those wavelengths are lower for E_d than L_u (47% vs. 56% and 36% vs. 50% for 443 and 490 nm, respectively -Fig. 6).

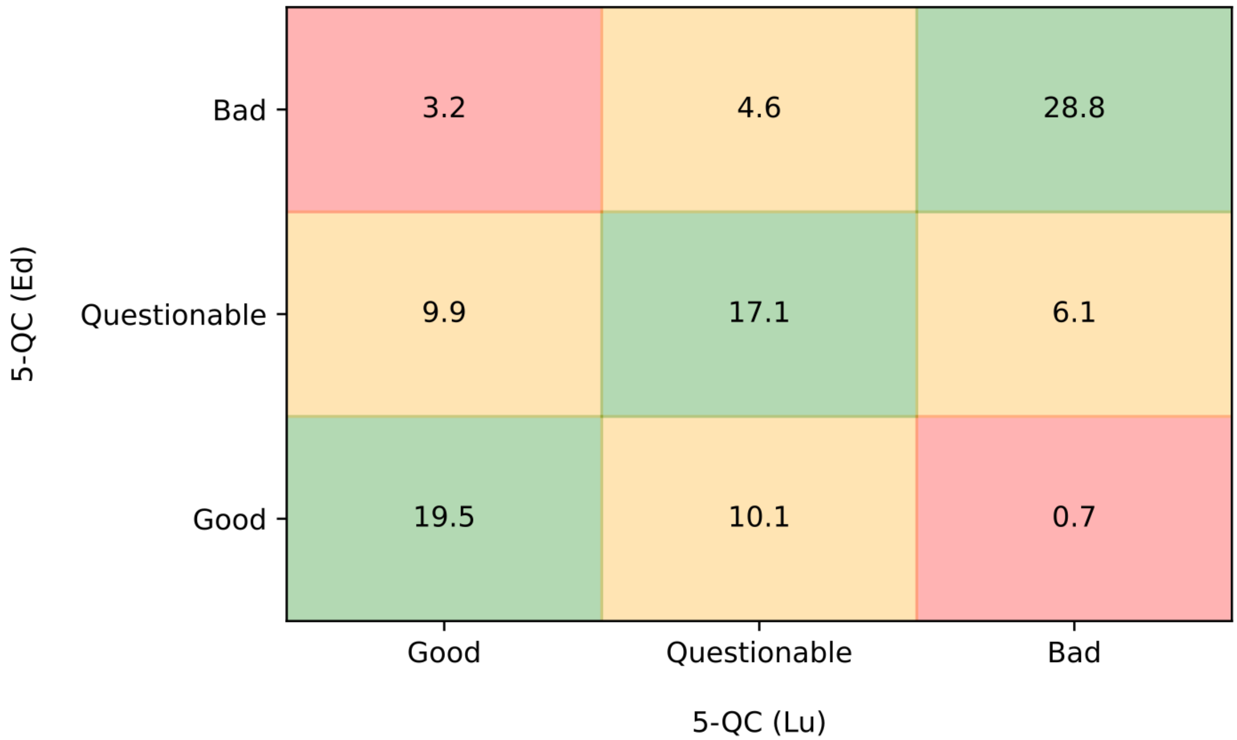

Fig. 7. Comparison matrix between QC classification of E_d profiles (on the y-axis) and QC classification of L_u profiles (on the x-axis). Green cells indicate the percentage of profiles for which the overall flag is the same for L_u and E_d; orange cells correspond to the percentage of profiles with a difference of only one QC level between E_d and L_u (e.g. Questionable/Bad or Good/Questionable); red cells represent the percentage of bad E_d profiles for good L_u profiles or vice versa.

Secondly, given that L_u refers to light going upward from the water, and that water itself strongly absorbs at larger wavelengths (>500 nm; Pope & Fry, 1997), the amount of upward light at those wavelengths is significantly lower than downwelling light, resulting in $E_d(\lambda>500) \gg L_u(\lambda>500)$ (Mobley, 2022). A small amount of light is not necessarily indicative of a lower signal; the TriOS radiometers modulate the integration time based on the amount of light, with a longer integration time leading to a stronger signal. This process is performed based on the channel that saturates first (usually the blue wavelength) (see details in Section 2.b; TriOS, 2025 and Mobley, 2022). As light penetrates deeper in the water column, given that red wavelengths attenuate faster than blue ones, the blue/red light ratio increases. Therefore, despite an increased integration time at depth (to keep the blue signal saturated), the red signal is lower, due to the faster decrease with depth.

A low signal, especially in the red, makes the fit performance worse (lower signal-to-noise ratio) and thus partly explains the larger amount of 'Bad' L_u profiles at 620 nm (Fig 6; Fig 7) than E_d profiles at 620 nm.

d. Comparison with established methods

To enable a more robust comparison of method performance, we applied all three classification approaches (the 3-wavelengths by (Organelli et al., 2016), 4-wavelengths by Wojtasiewicz et al., 2018, and the new 5-wavelengths methods) to the hyperspectral TriOS dataset. This is possible because the TriOS-RAMSES radiometers include all the relevant bands from both versions of the OCR-504 sensor. To directly compare the three method outputs, we computed a global flag after performing the 3-wavelengths and 4-wavelengths QC based on the proportion of Good/Questionable/Bad individual flags, following the percentages described in Section 3.d.

Overall, the QC distribution is consistent across the three methods (Fig. 8). The 5-QC classification aligns with the 3-QC 71.3% of the time and with the 4-QC at rates of 73.1% for E_d and 74.1% for L_u. Major differences in QC classification (type 1 vs. type 3) happened for 1.1%, 1.2%, and 0.9% of profiles, respectively. Most of the differences arise from the previous QC methods classifying profiles one level "better" than the 5-QC. For example, a profile categorized as "bad" by the 5-QC is often labeled as "questionable" by the 3-QC and 4-QC, while a "questionable" profile in our classification is frequently marked as "good" by the other two methods. The strong correlation between methods for the same profiles is also consistent with the RAMSES radiometer design, which relies on a single diffuser and thus can yield similar spectral responses (aside from effects related to wavelength-dependent light penetration). While the three quality control methods are largely similar, differing mainly in dark-signal and tilt detection and a slight variation in the r^2 cutoff value, we conclude that the primary source of their differences lies in the choice of wavelengths.

As discussed in Section 4.b. and 4.c, red wavelength profiles are unlikely to be impacted by weather phenomena when the float is at deeper depths (Fig. C1). However, they exhibit poor performance particularly for L_u (Fig. 6), owing to their lower signal-to-noise ratio compared to other parts of the spectrum, and the presence of inelastic scattering. These factors help explain part of the discrepancy in the overall quality assigned by the 5-QC compared to the 3-QC and the 4-QC approaches (Fig. 8). This highlights the importance of hyperspectral quality control to account for variability across the entire visible spectrum, as bio-physical disturbances do not have a uniform impact across wavelengths.

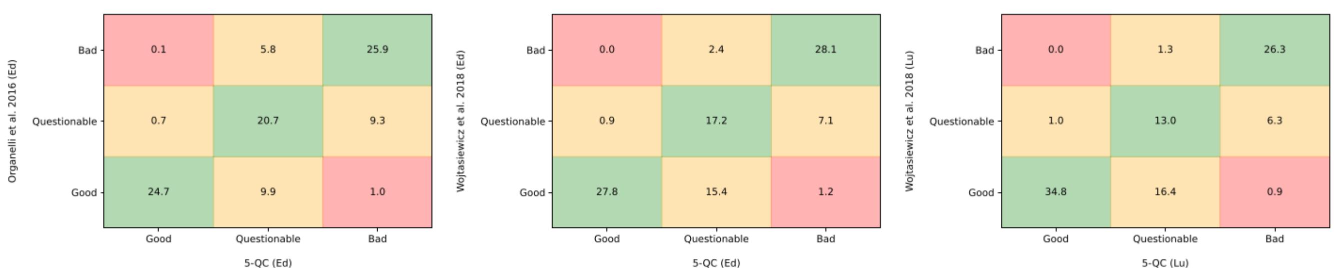

Fig. 8. Comparison matrix of 5-QC procedure with Organelli et al. 2016 method (3-QC, left panel) and Wojtasiewicz et al. 2018 method (4-QC, center panel) on E_d profiles. The right panel shows the comparison matrix of our QC procedure and Wojtasiewicz et al. (2018) method on L_u profiles.

e. Multispectral QC method for hyperspectral profiles

A comparison between the 5-QC and the Hyper-QC shows 69.1% and 70.5% of correspondence for E_d and L_u respectively. The significant correlation between the two methods shows that the 5-wavelengths chosen are representative of the full spectrum profile (Fig. 9). This strong correlation arises because the RAMSES radiometer is built with a single optical collector with an unique field of view. As a result, any wave-focusing effects—most pronounced in the upper layers—impact the signal across all wavelengths in a similar way, producing consistent responses throughout the spectrum and thus increasing the wavelength-to-wavelength correlation. Visualisations of the 3 profiles where the 5-QC and the Hyper-QC disagree are provided in Appendix C.

The main justification behind implementing the 5-QC method to QC hyperspectral data was to reduce computing costs and the effect of subjective threshold choices. Performing the QC over 5 wavelengths rather than 70 (or 140, depending on pixel settings) results in a computing time ~16x faster than doing it on the full set of wavelengths. Over the 899 profiles of the BGC-Argo dataset, this results in a ~2.5h run time for the 70-QC versus 12 minutes for the 5-QC (see Table 3).

Number of wavelengths in QC	Run time for 1 E_d+L_u pair (min)	Run time for 899 E_d+L_u pairs (min)
70	0.171	153
5	0.013	12
3	0.007	65

Table 3. Speed test of the computation of a wavelength-specific QC and the generation of a global spectrum flag for a single hyperspectral BGC-Argo float. The test was performed on a M1 Macbook, 16GB RAM. Each row refers to the amount of wavelength used to generate a global flag.

Although we have shown here that using the 5-QC represents a significant gain of time while providing thorough QC, for some applications interested in specific wavelengths of the spectra (e.g. chlorophyll-*a* natural fluorescence relative maximum at 690 nm, or hyperspectral K_d), it would be more appropriate to do a QC on the specific wavelengths of interest. The associated Python code was designed to allow for the user to easily modify both the number of wavelengths and the thresholds used.

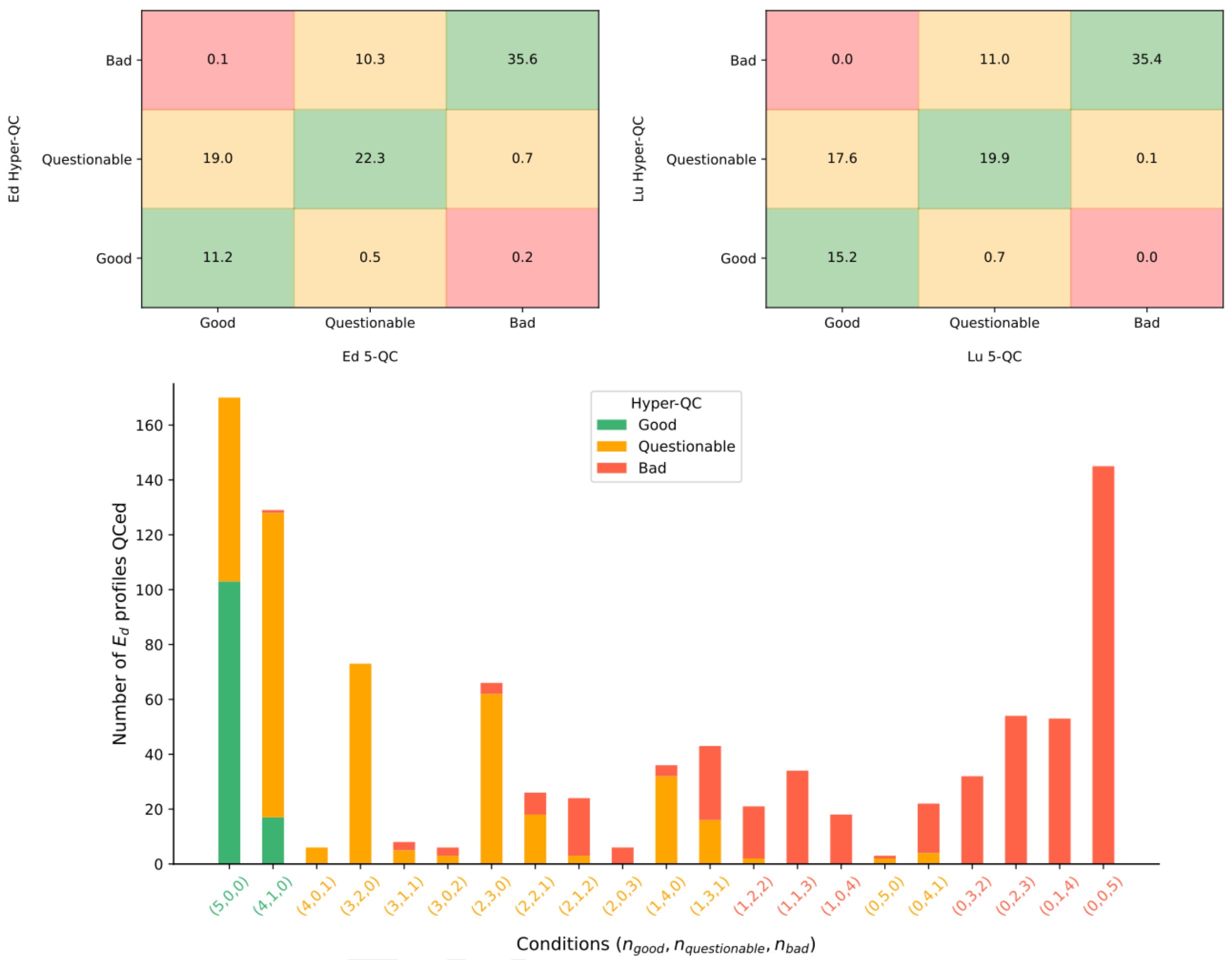

Fig. 9: At the top, a comparison table between the 5-QC and the Hyper-QC by overall type for both E_d (top left panel) and L_u profiles (top right panel). At the bottom, histogram of the distribution of the overall QC by conditions for the 5 wavelengths, colored by the hyperspectral QC result. The x-label colors correspond to the 5 wavelengths QC result. For example, the first x-tick is associated with the condition "(5,0,0)" which means: "5 wavelengths good, 0 wavelengths questionable and 0 wavelengths bad". It is written in green as it corresponds to a "Good" spectra for the 5-QC method. Among the ~170 profiles that meet this condition, ~100 of them are also flagged as "Good" by the 70-QC approach (green part of the bar) while ~70 of them are flagged as "Questionable" (orange part of the bar) and no "Bad" (red part of the bar).

When comparing the overall distribution of Good, Questionable, and Bad profiles depending on the amount of wavelengths used to perform the QC, we notice few differences in the overall distribution (Fig. 10), with the 5 wavelengths being slightly more stringent between Questionable and Bad.

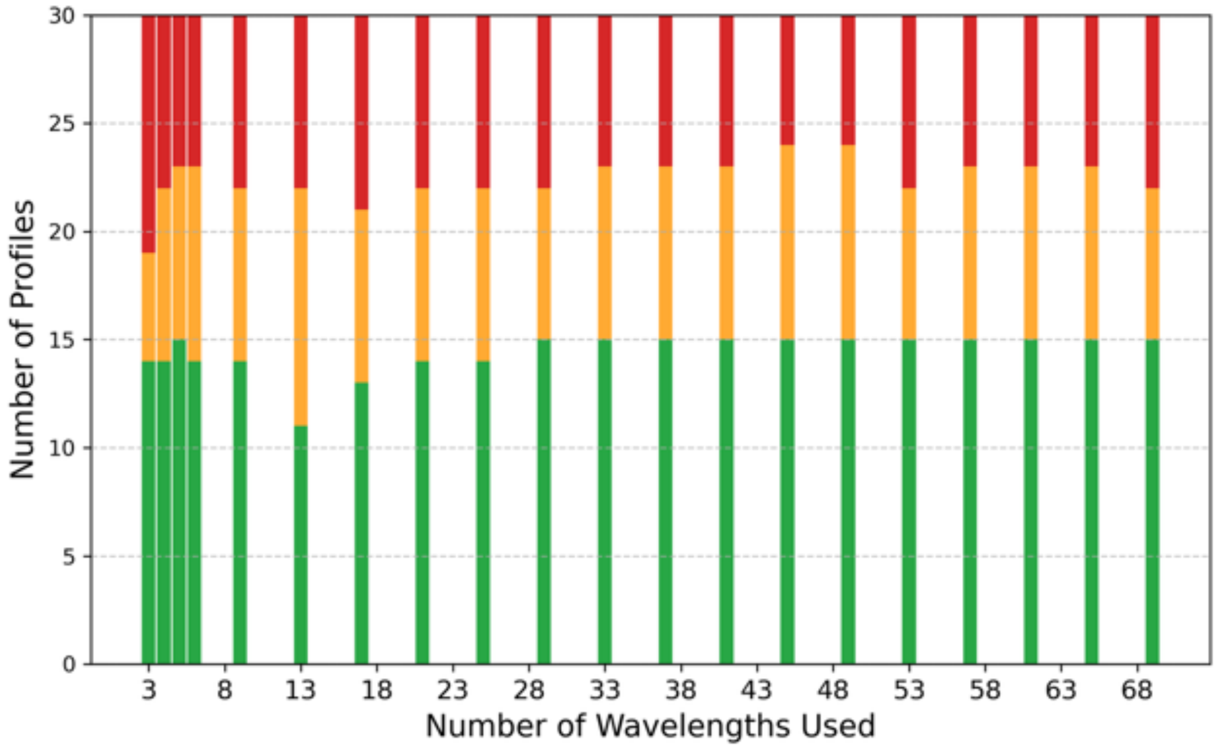

Fig. 10. The QC was performed on a varying number of wavelengths, ranging from 3 to 69, on 30 random profiles from float 2903787. The overall flag (Good, Questionable, Bad) was determined for a given profile based on the individual wavelengths' flags following the criteria described in section 3.e.

f. Profile depth qualification alternatives

In the method discussed in this paper, the quality control of radiometric profiles is performed over a different depth for each of the 5 reference wavelengths, depending on the amount of light that penetrates the water column (See Section 3.b). This allows the QC of the full profile, which is interesting for diffuse attenuation coefficient derivation and other variables related with biogeochemical properties (e.g. euphotic depth, PAR, isolume depth). However, this raises an issue about the consistency of weather conditions along the spectra. As the blue radiations penetrate the water deeper than the red ones, for example, a cloud passing when the float is between 150 and 100 m depth could affect the radiometric profile at 443 nm, that still can measure light at this depth, but not the 620 nm band, which has no light at this time and depth. For near-surface applications, it might be relevant to instead choose a constant depth for each wavelength. This threshold could be chosen as the minimum of the five wavelengths' penetration depths. The associated Python code allows for such modifications.

5. Conclusion

The BGC-Argo program has revolutionized our ability to observe biogeochemical processes on a global scale, providing unprecedented spatiotemporal coverage of essential ocean variables in regions that are otherwise undersampled (open-ocean gyres or southern ocean), overcoming some of the obstacles associated with traditional oceanographic cruises, such as bad weather conditions and high cost (Stoer et al., 2023). Since 2012, multispectral E_d measurements from Argo floats have contributed to populate a dataset of around ~60,000 profiles, spanning multiple oceanic regions and supporting a wide range of bio-optical studies (Organelli et al., 2017; Organelli & Claustre, 2019; Uitz et al., 2023). Notable applications include the SOCA (Satellite Ocean Color merged with Argo data to infer bio-optical properties to depth) methodology, which is based on an artificial neural network trained with E_d profiles acquired from BGC-Argo floats (Renosh et al., 2023) and the validation of remote sensing products such as remote sensing reflectance (Gerbi et al., 2016; Organelli, Barbieux, et al., 2017; Wojtasiewicz et al., 2018), K_d (Begouen Demeaux & Boss, 2022; Xing & Boss, 2021) and Chlorophyll concentration (Begouen Demeaux et al., 2025; Xing et al., 2011), demonstrating the value of these measurements for characterizing ocean optical properties (Jemai et al., 2021; Pitarch et al., 2025).

The quality of the BGC-Argo data for such applications relies on a dedicated QC methodology that can provide qualified profiles without operator control and independently of the weather conditions. As hyperspectral radiometers are now being integrated into the BGC-Argo fleet, ensuring the quality of these measurements is essential to fully realize their scientific potential. This study presents an automated, globally applicable quality-control methodology for hyperspectral E_d and L_u profiles that is independent of absolute light levels. Adapted from established multispectral approaches, the method reliably identifies sensor-related artifacts and unstable light conditions attributable to passing clouds, self-shading, large tilt angles, spikes, and wave focusing, enabling the robust use of hyperspectral radiometry for bio-optical applications. The associated Python implementation is openly available (https://gitlab.com/published-work-on-hyperspectral-bgc-argo/hyperspectral-5qc/), and hyperspectral K_d products derived using this framework have been released through SeaBASS (Haëntjens, 2022).

While additional factors such as sensor drift and biofouling, have not been addressed in this study, they remain critical for assessing the quality of radiometric measurements. Efforts have already been made to characterize them on multispectral sensors (Antoine et al., 2008; Jutard et al., 2021) and extending such analyses to hyperspectral instruments represents a valuable next step. In addition, wavelengths beyond 650 nm, which were not addressed in this paper, could be of particular interest for specific applications such as chlorophyll-*a* natural fluorescence or European Space Agency FLuorescence EXplorer satellite mission validation (Vicent et al., 2016). For these applications, adapted versions of the proposed quality-control approach could then be devised, replacing for instance, the polynomial fit with an approach that uses the chlorophyll-*a* concentration and Raman scattering estimations. Such developments would naturally benefit from a more detailed analysis of wavelength-to-wavelength correlations across the hyperspectral range following (Tan et al., 2024). In support of ocean-color satellite validation, particularly for new hyperspectral missions such as NASA's PACE, future work will focus on developing and releasing fully QCed datasets of L_w and R_{rs} derived from BGC-Argo hyperspectral floats.

Acknowledgments.

These data were collected and made freely available by the International Argo Program and the national programs that contribute to it. (https://argo.ucsd.edu, https://www.ocean-ops.org). The Argo Program is part of the Global Ocean Observing System.

This study is a contribution to the BGC-Argo-France (CNES-TOSCA) project.

The French Oceanographic Fleet provided support through ship time for the deployment of some floats used in this study.

This research receives financial support from the following projects and grants:

Argo-2030 has received the support of the French government within the framework of the "Investissements d'avenir" program integrated in France 2030 and managed by the Agence Nationale de la Recherche (ANR) under the reference "ANR-21-ESRE-0019".

The Euro-Argo ONE project has received funding from the European Union's Horizon Europe research and innovation programme under grant agreement no. 101188133.

The REFINE project has received funding from the European Research Council (ERC) under the European Union's Horizon 2020 research and innovation programme (grant agreement N° 834177).

The ITINERIS project has been funded by EU—Next Generation EU Mission 4 "Education and Research"—Component 2: "From research to business"—Investment 3.1: "Fund for the realization of an integrated system of research and innovation infrastructures"—Project IR0000032—ITINERIS—Italian Integrated Environmental Research Infrastructures System—CUP B53C22002150006. The authors acknowledge the Research Infrastructure Euro-Argo ERIC, participating in the ITINERIS project with its Italian node.

This research was supported by a NASA Future Investigators in NASA Earth and Space Science and Technology (FINESST) award (80NSSC24K1604) and the NASA PACE Validation & Science Team award (80NSSC24K0515) through funding from Centre National d'Etude Spatiale (CNES)

Data Availability Statement.

The associated Python script (https://gitlab.com/published-work-on-hyperspectral-bgc-argo/hyperspectral-5qc/) is freely available and customizable. The BGC-Argo hyperspectral profiles types (from 5QC method) until June 2025 for both Ed and Lu are made available in the Gitlab. A hyperspectral K_d product derived from E_d is downloadable in SEABASS (Haëntjens, 2022). E_d and L_u measurements by BGC-Argo floats in digital counts and in physical units are also available online at ftp://ftp.ifremer.fr/ifremer/argo/.

APPENDIX

Appendix A: Processing hyperspectral raw data for TriOS RAMSES mounted on Provor BGC-Argo floats

Raw data in counts (x) are converted into scientific units (y) using calibration coefficients (B0 and B1), integration time (t), and the calibration equations.

1. First, the background spectrum y_{dark} is calculated using dark calibration coefficients ($B0_{dark}$ and $B1_{dark}$ calculated as the average of the values measured by TriOs on the Dark pixels) also referred to as background coefficients in the manufacturer documentation. Then, we subtract the background from the normalized raw spectrum to obtain background-corrected measurement (y_{bc}).

$$y_{dark} = B0_{dark} + B1_{dark} * \frac{t}{8192}$$

$$y_{bc} = \frac{x}{65535} - y_{dark}$$

2. The dark signal (x_{dark}) -defined as the average of 17 black detector channels (TriOS, 2025)- is then retrieved from y_{bc} . Finally y_{bc} is adjusted for the sensor's calibration factor specific to seawater (S) defined by the manufacturer, and scaled to $\mu W.cm^{-2}.nm^{-1}$ or $\mu W.cm^{-2}.nm^{-1}.sr^{-1}$ to obtain E_d or L_u respectively in physical units (y_{phys}). No time interpolation is needed for the dark correction, given that the black channels are measured simultaneously as the rest of the spectrum.

$$y_{phys} = \frac{y_{bc} - \frac{1}{x_{dark}}}{S} * \frac{8192}{t}$$

Appendix B: Deriving heading from IMU raw data on Provor BGC-Argo floats.

To derive heading angle from IMU raw data, we apply the following equations, assuming the verticality of the float, using magnetometer raw data in digital counts (Mag_count_x, Mag_count_y, Mag_count_z), magnetometer calibration coefficients (m_{x0}, m_{y0} and m_{z0}) and compass calibration coefficients (h_1, h_2 si_{11}, si_{12}, si_{21} and si_{22}).

1. Orientation and simple calibration

$PhyMag_x$=Mag_count_x+m_{x0}

$PhyMag_y$=Mag_count_z+m_{z0}

$PhyMag_z$=Mag_count_y+m_{y0}

Note that the y axis of the IMU corresponds to the vertical axis of the float.

2. Compass calibration

$PhyMag_x$=$PhyMag_x$+hi_1

$PhyMag_y$=$PhyMag_y$+hi_2

F_$PhyMag_x$=$PhyMag_x$*si_{11} + $PhyMag_y$*si_{12}

F_$PhyMag_y$=$PhyMag_x$*si_{21} + $PhyMag_y$*si_{22}

3. Heading computation

heading = arctan(F_$PhyMag_y$, F_$PhyMag_x$) *180.0 / π

Appendix C: Examples of spectra with different results depending on QC method chosen

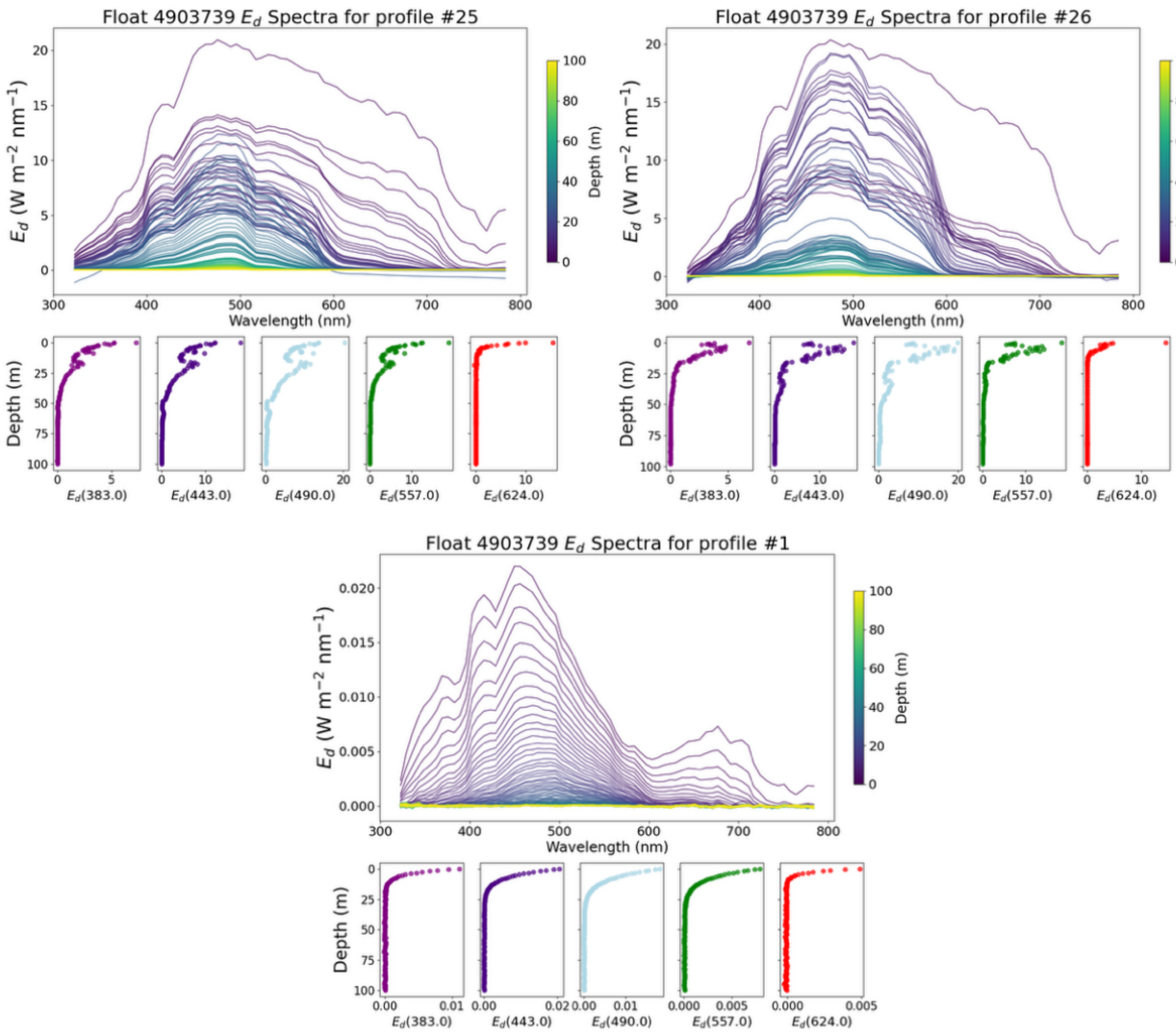

Figure C1. Examples of spectra for which the former QC did not result in the same result as the newly-developed 5-QC. In both examples above, profiles at the 441nm and the 487nm did not pass quality control. However, higher wavelengths (554 and 621 nm) do pass quality control, resulting in a different overall flag depending on which wavelengths are considered.

In this example, profiles 25 and 26 from float 4903739 failed the 5-QC but passed the Hyper-QC. Profile 25 is primarily affected by a pronounced spike at around 20 m depth, whereas profile 26 shows signatures consistent with wave focusing and the likely presence of a passing cloud. These perturbations mainly influence the blue–green wavelengths, thereby affecting most of the wavelengths used in the 5-QC. In contrast, they represent only a limited portion of the full hyperspectral range (320–700 nm) considered in the Hyper-QC. Moreover, relatively deep perturbations, such as the spike observed in profile 25, may be inconsequential for wavelengths that penetrate less deeply into the water column, as the disturbance occurs below the wavelength-dependent signal layer.

Conversely, profile 1 from float 4903739 is the only case in which the E_d profile passed the 5-QC but failed the Hyper-QC. In this instance, very low ambient light levels lead to a highly sensitive polynomial fit across all wavelengths, particularly in the near-UV and near-IR bands where the signal is weaker than in the blue-green bands. As a result, the profile marginally satisfies the 5-QC criteria, which emphasize blue–green wavelengths but fails the Hyper-QC which includes numerous wavelengths for which the signal is already strongly absorbed by water, yielding insufficient signal levels under these low-light conditions.

REFERENCES

Antoine, D., d’Ortenzio, F., Hooker, S. B., Bécu, G., Gentili, B., Tailliez, D., & Scott, A. J. (2008). Assessment of uncertainty in the ocean reflectance determined by three satellite ocean color sensors (MERIS, SeaWiFS and MODIS-A) at an offshore site in the Mediterranean Sea (BOUSSOLE project). *Journal of Geophysical Research: Oceans*, *113*(C7). https://doi.org/10.1029/2007JC004472

Barnard, A., Boss, E., Haëntjens, N., Orrico, C., Frouin, R., Tan, J., Klumpp, J., Dewey, M., Walter, D., Mazloff, M., & Chamberlain, P. (2024). Design and verification of a highly accurate in-situ hyperspectral radiometric measurement system (HyperNav). *Frontiers in Remote Sensing*, *5*. https://doi.org/10.3389/frsen.2024.1369769

Begouen Demeaux, C., & Boss, E. (2022). Validation of Remote-Sensing Algorithms for Diffuse Attenuation of Downward Irradiance Using BGC-Argo Floats. *Remote Sensing*, *14*(18), 4500. https://doi.org/10.3390/rs14184500

Begouen Demeaux, C., Boss, E., Graff, J. R., Behrenfeld, M. J., & Westberry, T. K. (2025). Phytoplanktonic Photoacclimation Under Clouds. *Geophysical Research Letters*, *52*(6), e2024GL112274. https://doi.org/10.1029/2024GL112274

Bittig, H. C., Maurer, T. L., Plant, J. N., Schmechtig, C., Wong, A. P. S., Claustre, H., Trull, T. W., Udaya Bhaskar, T. V. S., Boss, E., Dall’Olmo, G., Organelli, E., Poteau, A., Johnson, K. S., Hanstein, C., Leymarie, E., Le Reste, S., Riser, S. C., Rupan, A. R., Taillandier, V., … Xing, X. (2019). A BGC-Argo Guide: Planning, Deployment, Data Handling and Usage. *Frontiers in Marine Science*, *6*, 502. https://doi.org/10.3389/fmars.2019.00502

Bricaud, A., Babin, M., Morel, A., & Claustre, H. (1995). Variability in the chlorophyll-specific absorption coefficients of natural phytoplankton: Analysis and parameterization. *Journal of Geophysical Research: Oceans*, *100*(C7), 13321–13332.

https://doi.org/10.1029/95JC00463

Claustre, H., Johnson, K. S., & Takeshita, Y. (2020). Observing the Global Ocean with Biogeochemical-Argo. *Annual Review of Marine Science*, *12*(1), 23–48. https://doi.org/10.1146/annurev-marine-010419-010956

Donlon, C., Berruti, B., Buongiorno, A., Ferreira, M.-H., Féménias, P., Frerick, J., Goryl, P., Klein, U., Laur, H., Mavrocordatos, C., Nieke, J., Rebhan, H., Seitz, B., Stroede, J., & Sciarra, R. (2012). The Global Monitoring for Environment and Security (GMES) Sentinel-3 mission. *Remote Sensing of Environment*, *120*, 37–57. https://doi.org/10.1016/j.rse.2011.07.024

Gege, P., & Pinnel, N. (2011). Sources of variance of downwelling irradiance in water. *Applied Optics*, *50*(15), 2192–2203. https://doi.org/10.1364/AO.50.002192

Gerbi, G. P., Boss, E., Werdell, P. J., Proctor, C. W., Haëntjens, N., Lewis, M. R., Brown, K., Sorrentino, D., Zaneveld, J. R. V., Barnard, A. H., Koegler, J., Fargher, H., DeDonato, M., & Wallace, W. (2016). Validation of Ocean Color Remote Sensing Reflectance Using Autonomous Floats. *Journal of Atmospheric and Oceanic Technology*, *33*(11), 2331–2352. https://doi.org/10.1175/JTECH-D-16-0067.1

Gordon, H. R. (1979). Diffuse reflectance of the ocean: The theory of its augmentation by chlorophyll a fluorescence at 685 nm. *Applied Optics*, *18*(8), 1161–1166. https://doi.org/10.1364/AO.18.001161

Haëntjens, N. (2022). *PVST_VDIUP* (Version R1) [Dataset]. SeaWiFS Bio-optical Archive and Storage System (SeaBASS). https://doi.org/10.5067/SeaBASS/PVST_VDIUP/DATA001

Jemai, A., Wollschläger, J., Voß, D., & Zielinski, O. (2021). Radiometry on Argo Floats: From the Multispectral State-of-the-Art on the Step to Hyperspectral Technology. *Frontiers in Marine Science*, *8*. https://doi.org/10.3389/fmars.2021.676537

Johnson, K. S., & Claustre, H. (2016, November 8). *Bringing Biogeochemistry into the Argo Age*. Eos. https://eos.org/science-updates/bringing-biogeochemistry-into-the-argo-age

Jutard, Q., Organelli, E., Briggs, N., Xing, X., Schmechtig, C., Boss, E., Poteau, A., Leymarie, E., Cornec, M., D'Ortenzio, F., & Claustre, H. (2021). Correction of Biogeochemical-Argo Radiometry for Sensor Temperature-Dependence and Drift: Protocols for a Delayed-Mode Quality Control. *Sensors*, *21*(18), 6217. https://doi.org/10.3390/s21186217

La Forgia, G., & Organelli, E. (n.d.). Real-time quality assessment for Biogeochemical Argo radiometric profiles. *Limnology and Oceanography: Methods*, *n/a*(n/a). https://doi.org/10.1002/lom3.10701

Mobley, C. (with UNESCO/IOC, UNESCO/IOC, & Mobley, C.). (2022). *The Oceanic Optics Book* [924pp.]. International Ocean Colour Coordinating Group (IOCCG). https://repository.oceanbestpractices.org/handle/11329/1853

Morel, A., Gentili, B., Claustre, H., Babin, M., Bricaud, A., Ras, J., & Tièche, F. (2007). Optical properties of the "clearest" natural waters. *Limnology and Oceanography*, *52*(1), 217–229. https://doi.org/10.4319/lo.2007.52.1.0217

NOAA NCEI Geomagnetic Modeling Team; British Geological Survey. 2024: World Magnetic Model 2025. NOAA National Centers for Environmental Information.https://doi.org/10.25921/aqfd-sd83. Accessed 2026-06-23.

Ohde, T., & Siegel, H. (2003). Derivation of immersion factors for the hyperspectral TriOS radiance sensor. *Journal of Optics A: Pure and Applied Optics*, *5*(3), L12. https://doi.org/10.1088/1464-4258/5/3/103

Organelli, E., Barbieux, M., Claustre, H., Schmechtig, C., Poteau, A., Bricaud, A., Boss, E., Briggs, N., Dall'Olmo, G., D'Ortenzio, F., Leymarie, E., Mangin, A., Obolensky, G., Penkerc'h, C., Prieur, L., Roesler, C., Serra, R., Uitz, J., & Xing, X. (2017). Two databases derived from BGC-Argo float measurements for marine biogeochemical and bio-optical applications. *Earth System Science Data*, *9*(2), 861–880. https://doi.org/10.5194/essd-9-861-2017

Organelli, E., & Claustre, H. (2019). Small Phytoplankton Shapes Colored Dissolved Organic Matter Dynamics in the North Atlantic Subtropical Gyre. *Geophysical Research Letters*, *46*(21), 12183–12191. https://doi.org/10.1029/2019GL084699

Organelli, E., Claustre, H., Bricaud, A., Barbieux, M., Uitz, J., D'Ortenzio, F., & Dall'Olmo, G. (2017). Bio-optical anomalies in the world's oceans: An investigation on the diffuse attenuation coefficients for downward irradiance derived from Biogeochemical Argo float measurements: WORLD'S OCEAN BIO-OPTICAL ANOMALIES. *Journal of Geophysical Research: Oceans*, *122*(5), 3543–3564. https://doi.org/10.1002/2016JC012629

Organelli, E., Claustre, H., Bricaud, A., Schmechtig, C., Poteau, A., Xing, X., Prieur, L., D'Ortenzio, F., Dall'Olmo, G., & Vellucci, V. (2016a). A Novel Near-Real-Time Quality-Control Procedure for Radiometric Profiles Measured by Bio-Argo Floats: Protocols and Performances. *Journal of Atmospheric and Oceanic Technology*, *33*(5), 937–951. https://doi.org/10.1175/JTECH-D-15-0193.1

Organelli, E., Claustre, H., Bricaud, A., Schmechtig, C., Poteau, A., Xing, X., Prieur, L., D'Ortenzio, F., Dall'Olmo, G., & Vellucci, V. (2016b). A Novel Near-Real-Time Quality-Control Procedure for Radiometric Profiles Measured by Bio-Argo Floats: Protocols and Performances. *Journal of Atmospheric and Oceanic Technology*, *33*(5), 937–951. https://doi.org/10.1175/JTECH-D-15-0193.1

Organelli, E., Leymarie, E., Zielinski, O., Uitz, J., D'ortenzio, F., & Claustre, H. (2021). Hyperspectral Radiometry on Biogeochemical-Argo Floats: A Bright Perspective for

Phytoplankton Diversity. *Oceanography*, 90–91. https://doi.org/10.5670/oceanog.2021.supplement.02-33

Pitarch, J., Leymarie, E., Vellucci, V., Massi, L., Claustre, H., Poteau, A., Antoine, D., & Organelli, E. (2025). Accurate estimation of photosynthetic available radiation from multispectral downwelling irradiance profiles. *Limnology and Oceanography: Methods*, lom3.10673. https://doi.org/10.1002/lom3.10673

Pope, R. M., & Fry, E. S. (1997). Absorption spectrum (380–700 nm) of pure water II Integrating cavity measurements. *Applied Optics*, *36*(33), 8710. https://doi.org/10.1364/AO.36.008710

Poteau, A., Organelli, E., Boss, E., & Xing, X. (2019). *Quality control for BGC-Argo radiometry* (Version 1.0) [Pdf]. Ifremer. https://doi.org/10.13155/62466

Renosh, P. R., Zhang, J., Sauzède, R., & Claustre, H. (2023). Vertically Resolved Global Ocean Light Models Using Machine Learning. *Remote Sensing*, *15*(24), Article 24. https://doi.org/10.3390/rs15245663

Roemmich, D., Alford, M. H., Claustre, H., Johnson, K., King, B., Moum, J., Oke, P., Owens, W. B., Pouliquen, S., Purkey, S., Scanderbeg, M., Suga, T., Wijffels, S., Zilberman, N., Bakker, D., Baringer, M., Belbeoch, M., Bittig, H. C., Boss, E., … Yasuda, I. (2019). On the Future of Argo: A Global, Full-Depth, Multi-Disciplinary Array. *Frontiers in Marine Science*, *6*, 439. https://doi.org/10.3389/fmars.2019.00439

Shapiro, S. S., & Wilk, M. B. (1965). An analysis of variance test for normality (complete samples)†. *Biometrika*, *52*(3–4), 591–611. https://doi.org/10.1093/biomet/52.3-4.591

Stoer, A. C., Takeshita, Y., Maurer, T. L., Begouen Demeaux, C., Bittig, H. C., Boss, E., Claustre, H., Dall’Olmo, G., Gordon, C., Greenan, B. J. W., Johnson, K. S., Organelli, E., Sauzède, R., Schmechtig, C. M., & Fennel, K. (2023). A census of quality-controlled

Biogeochemical-Argo float measurements. *Frontiers in Marine Science*, *10*, 1233289. https://doi.org/10.3389/fmars.2023.1233289

Tan, J., Frouin, R., Häentjens, N., Barnard, A., Boss, E., Chamberlain, P., Mazloff, M., & Orrico, C. (2024). Reconstructing hyper-spectral downwelling irradiance from multi-spectral measurements. *Frontiers in Remote Sensing*, *5*. https://doi.org/10.3389/frsen.2024.1335627

Thode, H. C. (2002). *Testing For Normality*. CRC Press. https://doi.org/10.1201/9780203910894

TriOS. (2024). *RAMSES Hyperspectral radiometer Datasheet*.

TriOS. (2025). RAMSES technische spezifikationen. *TriOS Mess- und Datentechnik GmbH*. https://trios.de/ramses.html

Uitz, J., Roesler, C., Organelli, E., Claustre, H., Penkerc'h, C., Drapeau, S., Leymarie, E., Poteau, A., Schmechtig, C., Dimier, C., Ras, J., Xing, X., & Blain, S. (2023). Characterization of Bio-Optical Anomalies in the Kerguelen Region, Southern Indian Ocean: A Study Based on Shipborne Sampling and BioGeoChemical-Argo Profiling Floats. *Journal of Geophysical Research: Oceans*, *128*(12), e2023JC019671. https://doi.org/10.1029/2023JC019671

Vabson, V., Ansko, I., Duong, K., Vendt, R., Kuusk, J., Ruddick, K., Bialek, A., Tilstone, G. H., Gossn, J. I., & Kwiatkowska, E. (2024). Complete characterization of ocean color radiometers. *Frontiers in Remote Sensing*, *5*. https://doi.org/10.3389/frsen.2024.1320454

Vicent, J., Sabater, N., Tenjo, C., Acarreta, J. R., Manzano, M., Rivera, J. P., Jurado, P., Franco, R., Alonso, L., Verrelst, J., & Moreno, J. (2016). FLEX End-to-End Mission Performance Simulator. *IEEE Transactions on Geoscience and Remote Sensing*, *54*(7), 4215–4223. https://doi.org/10.1109/TGRS.2016.2538300

Wojtasiewicz, B., Hardman-Mountford, N. J., Antoine, D., Dufois, F., Slawinski, D., & Trull, T. W. (2018a). Use of bio-optical profiling float data in validation of ocean colour satellite products in a remote ocean region. *Remote Sensing of Environment*, *209*, 275–290. https://doi.org/10.1016/j.rse.2018.02.057

Wojtasiewicz, B., Hardman-Mountford, N. J., Antoine, D., Dufois, F., Slawinski, D., & Trull, T. W. (2018b). Use of bio-optical profiling float data in validation of ocean colour satellite products in a remote ocean region. *Remote Sensing of Environment*, *209*, 275–290. https://doi.org/10.1016/j.rse.2018.02.057

Wong, A. P. S., Wijffels, S. E., Riser, S. C., Pouliquen, S., Hosoda, S., Roemmich, D., Gilson, J., Johnson, G. C., Martini, K., Murphy, D. J., Scanderbeg, M., Bhaskar, T. V. S. U., Buck, J. J. H., Merceur, F., Carval, T., Maze, G., Cabanes, C., André, X., Poffa, N., … Park, H.-M. (2020). Argo Data 1999–2019: Two Million Temperature-Salinity Profiles and Subsurface Velocity Observations From a Global Array of Profiling Floats. *Frontiers in Marine Science*, *7*, 700. https://doi.org/10.3389/fmars.2020.00700

Xing, X., & Boss, E. (2021). Chlorophyll-Based Model to Estimate Underwater Photosynthetically Available Radiation for Modeling, *In-Situ* , and Remote-Sensing Applications. *Geophysical Research Letters*, *48*(7). https://doi.org/10.1029/2020GL092189

Xing, X., Morel, A., Claustre, H., Antoine, D., D’Ortenzio, F., Poteau, A., & Mignot, A. (2011). Combined processing and mutual interpretation of radiometry and fluorimetry from autonomous profiling Bio-Argo floats: Chlorophyll *a* retrieval. *Journal of Geophysical Research*, *116*(C6), C06020. https://doi.org/10.1029/2010JC006899

Zibordi, G., D’Alimonte, D., & Berthon, J.-F. (2004). *An Evaluation of Depth Resolution Requirements for Optical Profiling in Coastal Waters*.

https://journals.ametsoc.org/view/journals/atot/21/7/1520-0426_2004_021_1059_aeodrr_2_0_co_2.xml

Zibordi, G., Voss, K., Johnson, B. C., & Mueller, J. L. (2019). *IOCCG Ocean Optics and Biogeochemistry Protocols for Satellite Ocean Colour Sensor Validation, Volume 3.0: Protocols for Satellite Ocean Colour Data Validation: In Situ Optical Radiometry.* 67pp. http://dx.doi.org/10.25607/OBP-691